ORIGINAL PAPER

CrossMark

Experimental measurement of permeability evolution in sandstone during hydrostatic compaction and triaxial deformation

Jun Yu[1] · Weiya Xu[1] · Chaojun Jia[1] · Rubin Wang[1] · Huanling Wang[2]

Abstract
The permeability of sandstone during hydrostatic compaction and triaxial deformation was measured using a rock triaxial servo-controlled system. The gas permeability was also measured using an integrated permeability and porosity test system to study the difference between gas and water permeability. The experimental results suggested that gas permeability is larger than water permeability by almost one order of magnitude. This phenomenon is due to the slippage effect. The modified permeability is much closer to the water permeability. An empirical exponential relationship can describe the stress-dependent permeability of sandstone, while a power law is suitable to describe the relationship between porosity and effective confining pressure. During triaxial deformation, permeability initially decreases and then begins to increase at an accelerating rate. The peak value of permeability is hysteretic to peak stress. The initial permeability, lowest permeability, peak permeability, and stable value of permeability all decrease with the increase of effective confining pressure. The volumetric strain has a great effect on permeability. The turning point where permeability starts to increase coincides well with the onset of dilatancy.

Keywords Permeability · Hydrostatic compaction · Triaxial deformation · Strain · Effective confining pressure · Deviatoric stress

Introduction

Water and its seepage influence the stability and safety of large civil engineering projects. Due to different depths of stratum, stress relief, and the initiation and propagation of the excavation damage zone (EDZ), the surrounding rock is in complex stress states. According to statistics (Wu and Zhang 1995), 30–40% of dam collapse was induced by seepage. Therefore, it is significant and necessary to study the rock permeability during complex stress conditions.

The permeability of rock mass is closely related to the pore structures, and the development of pore structures relies on the stress states of rock mass. Therefore, researchers focused on the study of stress-dependent permeability and porosity (Athy 1930; Duan et al. 2014; Evans et al. 1997; Ghabezloo et al. 2009; Lion et al. 2004; Zoback and Byerlee 1975). Based on

laboratory work, some researchers suggested that the relationship between effective stress and permeability should follow an exponential relationship (David et al. 1994; Dong et al. 2010; Schmoker and Halley 1982; Wang et al. 2014b). However, Shi and Wang (1988) concluded that a power law was better for describing the stress-dependent permeability. Due to different rock types, structures, and experimental conditions, the best models to describe the stress-dependent permeability and porosity are still controversial issues.

When measuring permeability, both water and gas can be used as seepage media (Liu et al. 2017). Compared with water, inert gases have the following advantages: (1) wider in measuring range; (2) inert gases do not react with rock matrix; (3) the compressibility and viscosity of gas are less sensitive to temperature changes (Tanikawa and Shimamoto 2009). In this context, inert gas was widely used in the measurement of permeability (Liu and Shao 2017; Yuan et al. 2017). However, if gas is selected as the seepage medium, the test results may be higher than the intrinsic value because the slip of gas molecules on the pore walls may take place. In particular, this phenomenon is more significant when the radii of the pore throat are within the same order of magnitude as the mean free path of gas molecules. We should modify the test gas permeability to evaluate the intrinsic permeability

✉ Chaojun Jia
  jia-chao-jun@163.com

1 Research Institute of Geotechnical Engineering, Hohai University, Nanjing 210098, China

2 Key Laboratory of Coastal Disaster and Defense, Ministry of Education, Hohai University, Nanjing 210098, China

(Florence et al. 2007; Heid et al. 1950; Jones and Owens 1980; Sampath and Keighin 1982). The key to modifying the test permeability is to determine the slippage factor b. Based on a large amount of experimental data, the main achievements regarding the relationship between the slippage factor and the intrinsic permeability are given in Table 1. It can be seen that the slippage factor and the intrinsic permeability followed an exponential relationship. However, these empirical equations were obtained from specific rocks. Based on the result of Florence et al. (2007), Civan (2010) suggested that the slippage factor was in relation to $(K_\infty/\varphi)^{0.5}$ and can be described as $b = \frac{2.79\times10^3\mu}{\sqrt{M}}\left(\frac{K_\infty}{\varphi}\right)^{-0.5}$. This equation was found to agree well with various experimental data.

Compared with hydrostatic compaction, triaxial deformation results in the initiation, propagation, and coalescence of the microstructure of rock. Therefore, the permeability evolution in this process is not monotonous. The permeability evolution rules during the complete stress–strain process were studied by Alam et al. (2014), Heiland and Raab (2001), Mitchell and Faulkner (2008), and Wang et al. (2014a, 2015). Zhu and Wong (1996) considered that permeability was related to porosity, but the correlation between permeability and porosity before dilatancy of rock was not the same as that after dilatancy because of shear bands. Chen et al. (2014) suggested that permeability started to increase in the turning point of contraction and dilation. However, Mitchell and Faulkner (2008) concluded that permeability increased before the turning point based on the research of granodiorite. Wang et al. (2013) reached the same conclusion when testing the permeability of coal using CO_2. Due to variable ranges of permeability and different testing methods, different conclusions have been obtained. The permeability evolution rules are not clear, especially the permeability evolution in the post-peak region.

Therefore, in this paper, to study the permeability of sandstone under hydrostatic compaction, permeability under different confining pressures was measured with the steady-state method. Both distilled water and inert gas were selected as the seepage media. Based on the experimental results, the difference between the test gas permeability and water permeability was discussed. Meanwhile, permeability was measured during the complete stress–strain process with confining pressures of 4, 6, and 8 MPa. The permeability evolution rules during different stages were discussed. The influence of volumetric strain on permeability were also studied in this paper.

Experimental methodology

Description of the rock samples

The sandstone used in this paper was from a hydropower station in southwest China. The mean density of the sandstone with the initial average porosity of 8.43% was 2.23 g/cm^3. The microstructure was identified using a scanning electron microscope (SEM) with X-ray energy dispersive spectroscopy. Before testing, a thin section of rock which was cut randomly from a rock mass was prepared. The composition of this sandstone is 39.2% SiO_2, 12.77% Al_2O_3, and a small amount of MgO, Fe_2O_3, CaO, etc. The SEM images with different magnifications are shown in Fig. 1. From the lower magnification image (×500), we can see that the grains of sandstone are tightly cemented together. Some primary intergranular porosity is uniformly distributed in the sample. However, the higher magnification image (×3500) shows that euhedral quartz grows in the detrital quartz, which fills most of the pores. Part of the small pores also connects, which develops into microcracks. The microcracks and pores in the thin section form flow channels for the seepage medium.

The rock samples used for the experiments were cylindrical cores of 50 mm in diameter and 100 mm in length, according to the rock mechanics regulations (GB/T50266-2013). Samples were saturated for 24 h before the experiments. When testing with gas, the samples should be cut into 50-mm lengths to adjust to the equipment. Samples were also needed to be dried at a temperature 105 °C until they reached a constant mass.
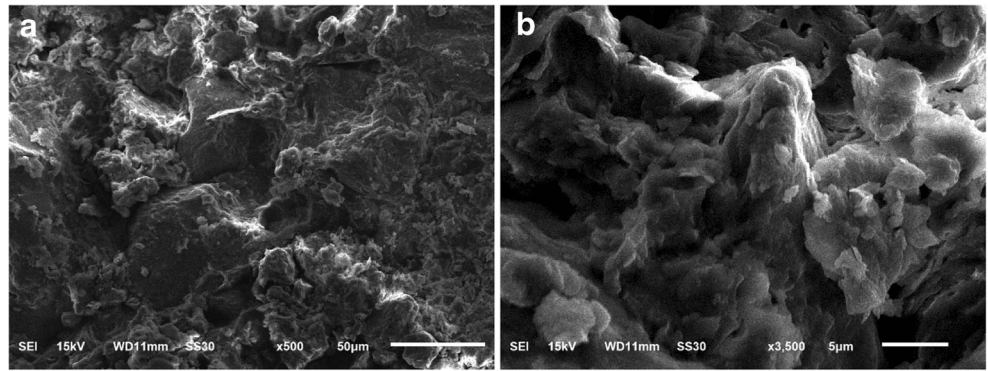
Experimental system and method

The rock triaxial servo-controlled system and the integrated permeability and porosity system were used to test permeability under triaxial deformation and hydrostatic deformation.

Permeability under triaxial deformation

The schematic diagram of the rock triaxial servo-controlled system is shown in Fig. 2. This apparatus utilizes three separate servo pumps to generate confining stress, deviatoric stress, and pore pressure, respectively. The maximum loading capacities of the three pumps are 60, 300, and 60 MPa,

Table 1 Relationship between the slippage factor and the intrinsic permeability

Author	Equation	Material
Heid et al. (1950)	$b = 11.419k_\infty^{-0.39}$	11 synthetic cores and 164 natural cores
Jones and Owens (1980)	$b = 12.639k_\infty^{-0.33}$	More than 100 samples from tight gas sands
Sampath and Keighin (1982)	$b = 13.851(k_\infty/\varphi)^{-0.53}$	10 core samples from a tight gas sand field
Florence et al. (2007)	$b = \rho(k_\infty/\varphi)^{-0.5}$	Capillary model

Fig. 1 Scanning electron microscope (SEM) images of sandstone

respectively. Axial displacement is monitored by two linear variable displacement transducers (LVDT), placed on either side of the sample. Lateral strain is determined by a radial strain gauge wrapped tightly around the central part of the sample. All of the experimental data are recorded by a computer and displayed on a monitor in real time.

For permeability testing under triaxial deformation with water, the test procedure was as follows. (1) The sample was wrapped by a Vitton jacket and hooped tightly in the triaxial cell. (2) Confining pressure P_c and upstream pressure P_u were loaded to the desired values successively and the downstream side was connected to atmosphere. This state should be held until water flowed out of the downstream side. (3) Deviatoric stress was applied at a rate of 0.75 MPa/min until the sample failed. Based on the recorded quality of water, the steady-state flow method was employed to assess the permeability of sandstone.

Permeability under hydrostatic compaction

An integrated permeability and porosity system was utilized to measure the gas flow property of sandstone samples (see Fig. 3). To measure gas permeability, the sample was placed in the hydrostatic cell. The confining pressure was supplied with a confining pump. A gas reservoir was plugged on the upstream side of the sample in order to ensure a relatively

Fig. 2 Schematic diagram of the experimental apparatus

stable upstream pressure. The upstream pressure can be measure by *Manometer 2*. Initially, pure gas with pressure P_1 was injected to the upstream side of the sample. According to Darcy's law, gas permeability can be deduced with a small decrease in upstream pressure ΔP during time variation Δt; see Loosveldt et al. (2002) for further details on the derivation:

$$K_{eff} = \frac{2\mu_g h Q P_{mean}}{A\left(P_{mean}^2 - P_0^2\right)} \quad (1)$$

where K_{eff} is the permeability measured by gas (m^2); A and h are the cross-sectional area and height of the sample, respectively; μ_g is the viscosity coefficient of the gas; P_0 is atmospheric pressure (0.1 MPa); and P_{mean} is the mean pressure, which is equal to $(P_1 - \Delta P/2)$ (MPa). According to the law of conservation of mass, the mass of gas which flows from the upstream side should be equal to that which flows through rock samples during time Δt. In such a context, the gas flow rate Q is:

$$Q = \frac{V_0 \Delta P}{P_{mean} \Delta t} \quad (2)$$

where V_0 is the total volume of the upstream side (m^3). Equation (1) is the steady-state method that is widely used in permeability measurement. Permeability measurement relates to the upstream gas flow rate Q. If the sample is too compact to let the gas flow through it, the variation of upstream pressure ΔP is difficult to record. In order to resolve this problem, a high-precision *Manometer 2* is installed in the downstream side of the sample. Its variation value is recorded during time Δt. Then, the gas flow rate can be expressed as:

$$Q = \frac{V_s \Delta P'}{\Delta t\left(P_0 + \Delta P'/2\right)} \quad (3)$$

where V_s is the dead volume of the downstream side. Due to the smaller volume V_s than the upstream side, the pressure variation $\Delta P'$ measured by *Manometer 2* during time variation Δt is more significant than ΔP. Therefore, this method is more accurate and can shorten the testing time compared with the conventional steady-
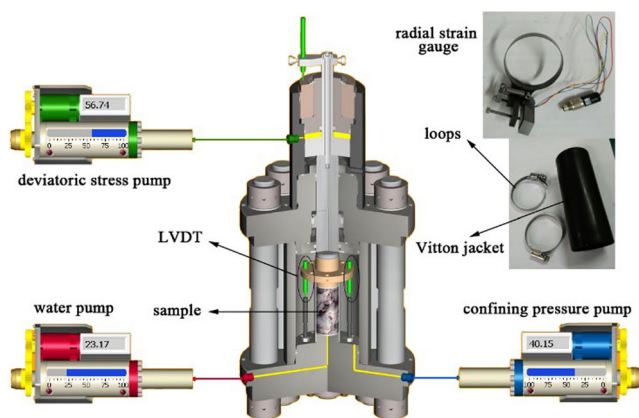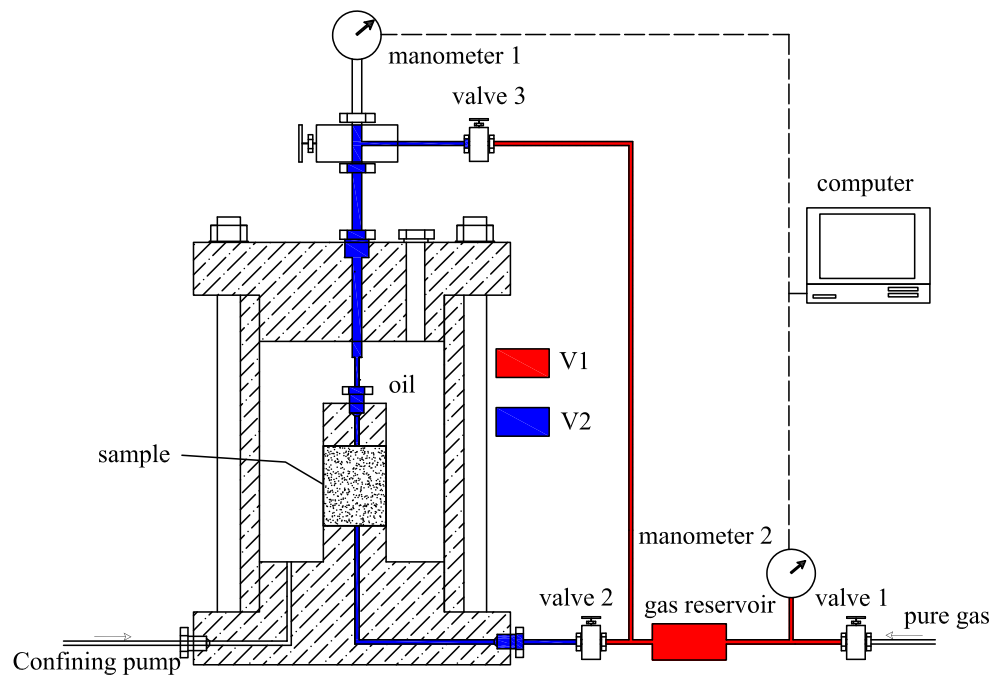
Fig. 3 Schematic diagram of the permeability and porosity test system

state method. In this context, the permeability of sandstone sample can be calculated as:

$$K_{eff} = \frac{2\mu_g hQP_0}{A(P_1^2 - P_0^2)} \quad (5)$$

Before measuring porosity, a steel sample with the same dimensions as the rock sample was placed inside the cell to measure the dead volume V_1 and V_2. When testing porosity, the sample was isolated from the gas through closing *Valve 2* and *Valve 3*. The gas pressure P_{ini} was recorded in this process. Secondly, the two valves were opened to inject the gas into the sample from the two end surfaces. Finally, a new stable gas pressure P_{end} corresponding to the volume $V_1 + V_2 + V_v$, where V_v is the sample pore volume, was reached. According to the law of conservation of mass of perfect gas, the following is obtained (Wang et al. 2017):

$$P_{ini}V_1 = P_{end}(V_1 + V_2 + V_{v'}) \quad (6)$$

In this context, the porosity of sandstone is given by $\varphi = V_v/V_s$, where V_s is the volume of the sample.

The permeability and porosity were measured under each confining pressure. The confining pressure was gradually increase from 3 to 30 MPa. The specific testing programs are listed in Table 2. In order to compare with the gas permeability, the permeability was also measured by water with confining pressure increases step by step.

Experimental results and discussion

Permeability under hydrostatic compaction

Figure 4 shows the evolution of water permeability with the increase of effective confining pressure. The effective confining pressure is defined as the difference between the confining pressure P_c and the pore pressure P_p. When measuring permeability using the steady-state method, the effective confining pressure can be expressed as:

$$P_e = P_c - P_p = P_c - \frac{P_{up}}{2} \quad (7)$$

The upstream pressure P_{up} is equal to 1 MPa. From Fig. 4, we can see that, with the increase of stress, the closure of preexisting pores and microcracks leads to the decrease of permeability. Compared with pores, microcracks are more sensitive to stress and are more able to let water flow through the sample. The closure of microcracks occurs firstly. The permeability falling rate thus decreases with the effective confining pressure. After measuring the porous

Table 2 Descriptions of the test programs

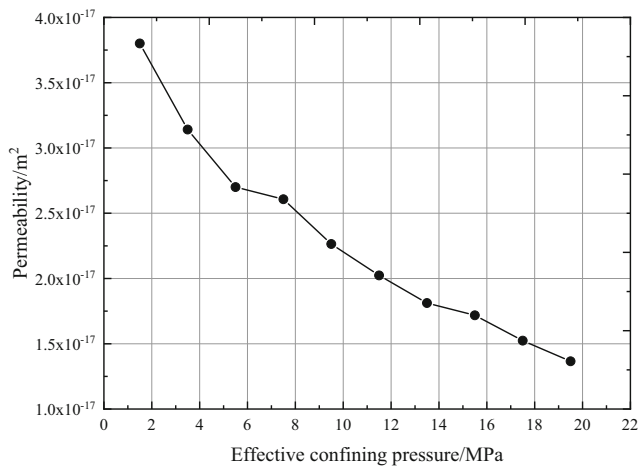| Test type	Seepage medium	P_c (MPa)	P_p (MPa)
Triaxial deformation	Distilled water	4	0.5
Triaxial deformation	Distilled water	6	0.5
Triaxial deformation	Distilled water	8	0.5
Hydrostatic compaction	Distilled water	2–20	0.5
Hydrostatic compaction	Argon	3–30	0.5

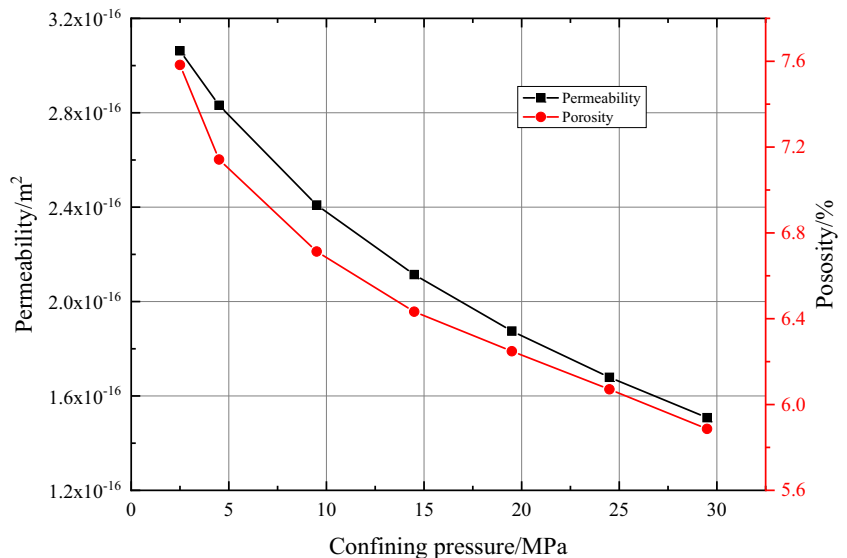**Fig. 4** Water permeability under increasing effective confining pressure

volume and the volume deformation of the samples, Wang et al. (2017) pointed out that the closure of microcracks and pores is progressive and the transition depends on the skeleton modulus and the confining pressure.

Figure 5 shows the gas permeability and porosity variation with the increase of the effective confining pressure. Both permeability and porosity decrease with the stress. Compared with permeability, porosity reduces quickly when the stress increases from 2.5 to 4.5 MPa, and then becomes less sensitive to the stress increasing. Regardless of whether the seepage medium is water or gas, the stress-dependent permeability evolution rules are similar.

Modifying gas permeability

When gas flows through low-permeability rocks, the pore throat sectional area is within two orders of magnitude of the mean free path of the gas molecules and the gas molecules will slip on the surface of the pores. This phenomenon, which adds

additional value to testing permeability, is called the Klinkenberg effect. Klinkenberg (1941) proved that there exists a linear relationship between gas permeability and reciprocal mean pressure between upstream and downstream $1/\overline{P}$, and the relationship between gas permeability and intrinsic permeability can be expressed as:

$$K_g = K_\infty \left(1 + \frac{b}{\overline{P}} \right) \tag{8}$$

where K_g is the measured gas permeability (m^2) and K_∞ is the intrinsic permeability (m^2). Therefore, the key to modifying permeability is to obtain the slippage factor b. The slippage factor b, related to the temperature, gas type, and pore structure of porous media, can be calculated as (Civan 2010):

$$b = \frac{4c\lambda\overline{P}}{r} \tag{9}$$

where c is a constant (the general value is 1); λ is the mean free path of gas molecules (m); ad r is the pore throat sectional area (m), which cannot be measured directly. During the study of the slippage factor, Civan (2010) concluded that the slippage factor related to intrinsic permeability and initial porosity can be expressed as:

$$b = \frac{2.79 \times 10^3 \mu}{\sqrt{M}} \left(\frac{K_\infty}{\varphi} \right)^{-0.5} \tag{10}$$

where M is the molecular weight of the gas (kg/kmol). This equation is used to modify gas permeability in this paper. When the gas used is Argon, Eq. (10) can be expressed as:

$$b = 9.7 \times 10^{-9} \left(\frac{K_\infty}{\varphi} \right)^{-0.5} \tag{11}$$

Fig. 5 Gas permeability and porosity under increasing effective confining pressure

Therefore, combining Eqs. (8) and (11), the intrinsic permeability can be calculated as listed in Table 3. It can be seen that the slippage effect has a great influence on gas permeability. The modified permeability is much smaller than the gas permeability. The gap between gas permeability and modified values increases with the increase of effective confining pressure. For example, when the stress is 2.5 MPa, the gas permeability is 9.6 times the modified value. However, when the stress is 29.5 MPa, the gas permeability can reach up to 17.6 times the modified permeability.

Difference between water permeability and modified gas permeability

Figure 6 shows the difference between the water permeability and the modified gas permeability of sandstone. It is obvious that the modified gas permeability is not much different from the water permeability. In addition, they have similar variation trends. The water permeability tends to be a litter higher than the modified one. This result was also proposed by Tanikawa and Shimamoto (2009), who considered that the gas viscosity was closely related to the pore pressure, which would increase the measured gas permeability. In addition, water dissolves the matrixes of sandstone, which expands the pore throat radius and makes a contribution to water permeability.

Stress-dependent permeability and porosity

The stability assessment of large civil engineering projects requires a clear relationship between permeability and strata depths. David et al. (1994) suggested that an exponential equation can reflect the relationship between permeability and effective confining pressure. Such an exponential relationship can be expressed as:

$$K = K_0 exp[-\gamma(P_e-P_0)] \tag{12}$$

where K is the permeability under the effective confining pressure P_e (m^2); K_0 is the permeability under atmospheric pressure P_0 (0.1 MPa); and γ is a material constant (MPa^{-1}). However, Shi and Wang (1988) suggested that a power law is more appropriate to describe stress-dependent permeability and the equation can be expressed as:

$$K = K_0 \left(P_e/P_0\right)^{-\beta} \tag{13}$$

where β is a material constant. Based on the laboratory permeability test results, both water permeability and modified gas permeability are fitted curves using Eqs (12) and (13). The fitting parameters are given in Table 4. The results show that the determined parameters of the exponential relationship are $K_0 = 3.86 \times 10^{-17}$ m^2 and $\gamma = 0.054$ MPa^{-1}. For the power law, the determined parameter K_0 is 1.44×10^{-17} m^2 and β is 0.427. When the stress is less than 19.5 MPa, the power law

can better simulate the modified gas permeability. However, the curve will deviate from the actual value with the increasing of stress. Generally, the exponential relationship can better simulate the stress-dependent permeability of sandstone.

Hoholick et al. (1984) suggested that the relationship between the porosity of sandstone and effective confining pressure can be expressed as an exponential relationship:

$$\varphi = \varphi_0 exp[-\alpha(P_e-P_0)] \tag{14}$$

where φ is the porosity under the effective confining pressure P_e (m^2); φ_0 is the porosity under atmospheric pressure P_0; and α is a material constant (MPa^{-1}). The parameters determined for the sandstone are $\varphi_0 = 7.520\%$ and $\alpha = 8.92$ MPa^{-1}. The power law is better at describing the relationship between porosity and effective confining pressure, which is different from permeability:

$$\varphi = \varphi_0 \left(P_e/P_0\right)^{-\theta} \tag{15}$$

where θ is a material constant. This determined parameter θ is 0.105 for sandstone. The initial porosity φ_0 is equal to 10.892%, which is an overestimate compared with the measured result.

Permeability under triaxial deformation

Figure 7 shows the experimental results of the permeability measurement during the complete stress–strain process under different confining pressures. It should be noted that the permeability of sandstone was tested in the post-peak region. The confining pressures were 4, 6, and 8 MPa, and the upstream pressures were all equal to 1 MPa.

Based on the experimental results, the stress–axial strain curves can be divided into five stages: initial compression stage, linear elastic deformation stage, yield stage, post-failure stage, and residual deformation stage. During the initial compression stage, the stress–stain curve is concave upwards, which indicates that the stiffness increases with the applied stress. In addition, the concave upwards stage is more significant under lower confining pressures. During the linear elastic deformation stage, all curves appear to be linear up until the yield point, where the curves deviate from the linear trend. The peak stresses are 84.26, 107.08, and 120.50 MPa for effective pressures of 3.5, 5.5, and 7.5 MPa, respectively. In the post-failure stage, strain softening takes place and the stress becomes stable in the residual deformation stage.

Compared with the stress–axial strain curves, the stress–lateral strain curves increase almost linearly in the first two stages. In the yield stage, the lateral strain expands rapidly. The lateral strain is more sensitive than the axial strain to the increase of deviatoric stress. When the curves approach the peak stress, the lateral strains becomes almost horizontal. All of the lateral curves under different effective confining

Table 3 Gas permeability and its modified values under different effective confining pressures

Confining pressure (MPa)	Pore pressure (MPa)	Gas permeability (m²)	Modified permeability (m²)
3	0.5	3.06×10^{-16}	3.19×10^{-17}
5		2.83×10^{-16}	2.77×10^{-17}
10		2.41×10^{-16}	2.06×10^{-17}
15		2.11×10^{-16}	1.62×10^{-17}
20		1.87×10^{-16}	1.29×10^{-17}
25		1.68×10^{-16}	1.05×10^{-17}
30		1.51×10^{-16}	8.58×10^{-18}

Fig. 6 The relationship between permeability (**a**), porosity (**b**), and effective confining pressure

$$K = 3.86 \times 10^{-17} \exp\left[-0.054\left(P_e - P_0\right)\right]$$
$$R^2 = 0.978$$

$$K = 1.44 \times 10^{-16}\left(P_e / P_0\right)^{-0.427}$$
$$R^2 = 0.932$$

$$\varphi = 7.520\% \exp\left[-8.92 \times 10^{-3}\left(P_e - P_0\right)\right]$$
$$R^2 = 0.923$$

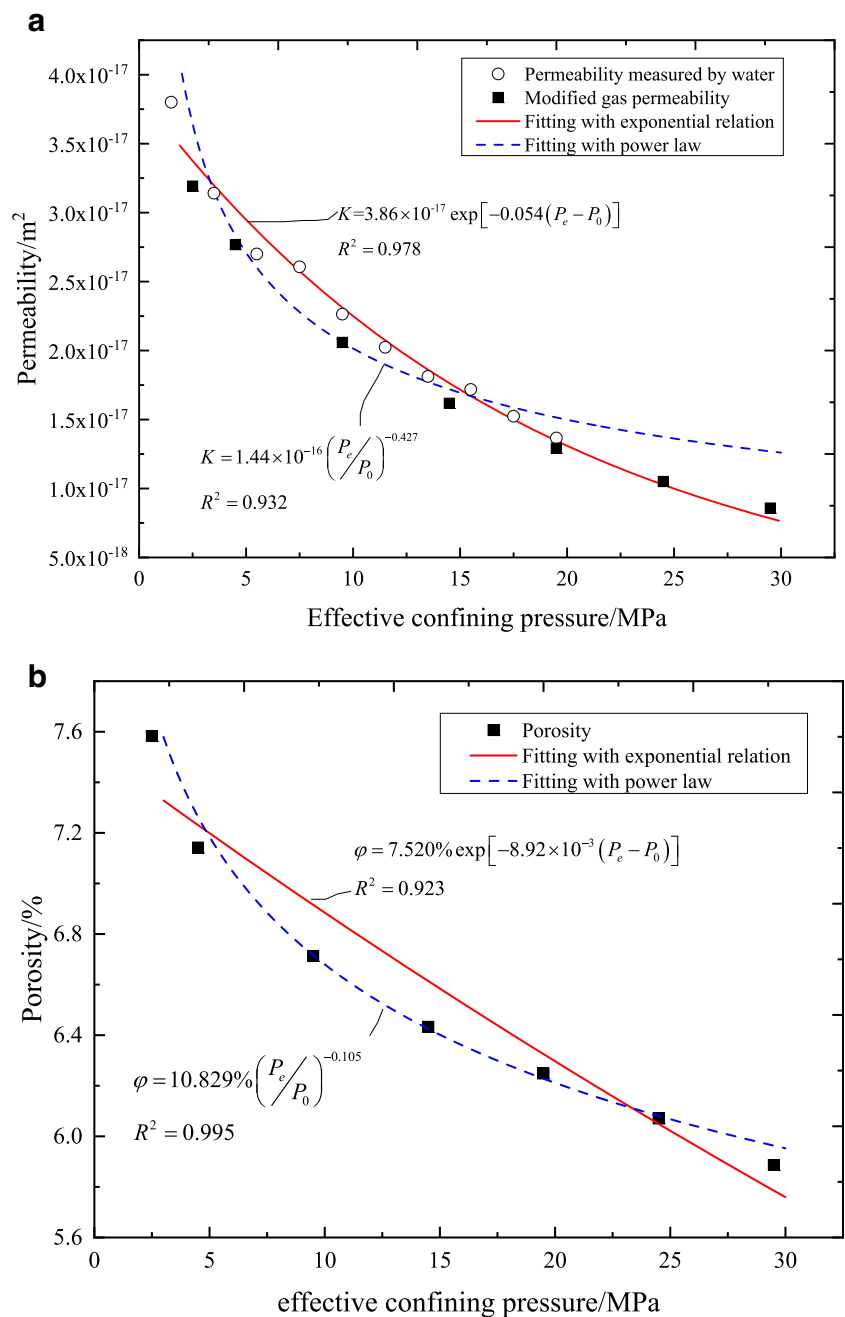$$\varphi = 10.829\%\left(P_e / P_0\right)^{-0.105}$$
$$R^2 = 0.995$$

Table 4 Parameters determined using a fitting curve based on the water permeability and modified gas permeability and porosity of sandstone

Permeability				Porosity			
Exponential relationship		Power law		Exponential relationship		Power law	
K_0 (m^2)	γ (MPa^{-1})	K_0 (m^2)	β	φ_0 (%)	α (MPa^{-1})	φ_0 (%)	θ
3.86×10^{-17}	0.054	1.44×10^{-16}	0.427	7.520	8.92×10^{-3}	10.829	0.105
$R^2 = 0.978$		$R^2 = 0.932$		$R^2 = 0.923$		$R^2 = 0.995$	

pressures dilate until reaching stable values after failure of the sample. The volumetric strains show that the sandstone volume changes from contraction to dilation as the deviatoric stress increases. During the residual deformation stage, a small contraction occurs.

The initial permeabilities of the three samples are 2.92×10^{-17}, 2.74×10^{-17}, and 2.61×10^{-17} m^2, respectively. The results show that the initial permeability decreases with the increase of effective confining pressure. As strain increases, the permeability decreases gradually. However, the boundary between the initial compression stage and the linear elastic deformation stage is not apparent. For an effective confining pressure of 3.5 MPa, the permeability increases up to the peak stress, after which there is a steady decrease. The increase rate is relatively slow compared with that after the sample loses its bearing capacity.

The peak value of permeability varies from the lowest of 1.18×10^{-17} to 8.39×10^{-16} m^2, a nearly two orders of magnitude change. The ultimate stable permeability is 3.58×10^{-17} m^2. For effective confining pressures of 5.5 and 7.5 MPa, the variation of permeability is shown to be identical. All samples show that the peak values of permeability lag behind peak stresses. With strain increases, the permeability decreases during the residual deformation stage. For an effective confining pressure of 5.5 MPa, the permeability varies from 1.02×10^{-17} m^2 to 5.72×10^{-16} m^2. For an effective confining pressure of 7.5 MPa, the permeability increases from 9.30×10^{-18} m^2 to 1.78×10^{-16} m^2. Therefore, both the lowest and peak permeabilities decrease with the increase of effective confining pressure. The ultimate steady permeability, which ranges from 2.82×10^{-16} to 5.00×10^{-17} m^2 for effective confining pressures of 5.5 and 7.5 MPa, respectively, shows the same evolution rule.

The relationship between permeability and axial strain under triaxial deformation

The stress–axial strain curves in the process of deformation and failure can be divided into five stages. The evolution of permeability is limited in the initial compression stage and linear elastic deformation stage. However, the permeability changes from decrease to increase when the samples yield. In addition, the permeability increasing rate rises rapidly after samples failure. Based on laboratory results, permeability evolution can be divided into the following stages.

Permeability corresponds to the OA segment of the stress–axial strain. During this stage, the permeability is very low. From the SEM test, we can see that the porous media, sandstone, contains a large number of defects (microcracks and pores), and the distribution of the defects is random. The initial permeability variation is similar to the result of hydrostatic compaction, which is induced by effective confining pressure. When deviatoric stress is applied to the sample, the defects perpendicular to the applied stress shrink further with the re-arrangement of sandstone grains, which blocks the flow paths of water. With the increasing of deviatoric stress, the coalescence of new generated microcracks forms flow channels.. When the newly formed microcracks are in dominated role, the permeability increases. The seepage during this stage is dominated by pore flow, so the permeability is relatively low.

Permeability corresponds to the AB segment of the stress–axial strain. During this stage, the permeability increases rapidly. Initial microcracks propagating with sandstone grains extrude together, which forms transgranular fractures. With the effect of deviatoric stress, microcracks are directionally arranged along the shear plane. If the samples reach the critical crack density, irreversible failure occurs quickly. The fractures become the main seepage channels. The permeability increases sharply due to the connected fractures. The restraint of effective confining pressure results in the decrease of peak permeability with the effective confining pressure. In addition, the permeability, which is reflected in the changes of pore structures induced by rock deformation, appears to be hysteretic compared with the peak stress.

Permeability corresponds to the BC segment of the stress–axial strain. During this stage, the permeability decreases and tends to be stable. The slipping and closing of fractures are followed by the filling of friction grains, and permeability decreases.

The relationship between permeability and volumetric strain

Axial strain was measured by LVDT in this paper, and lateral strain was measured by a radial strain gauge placed in the central part of the sample. The volumetric strain can be calculated by:

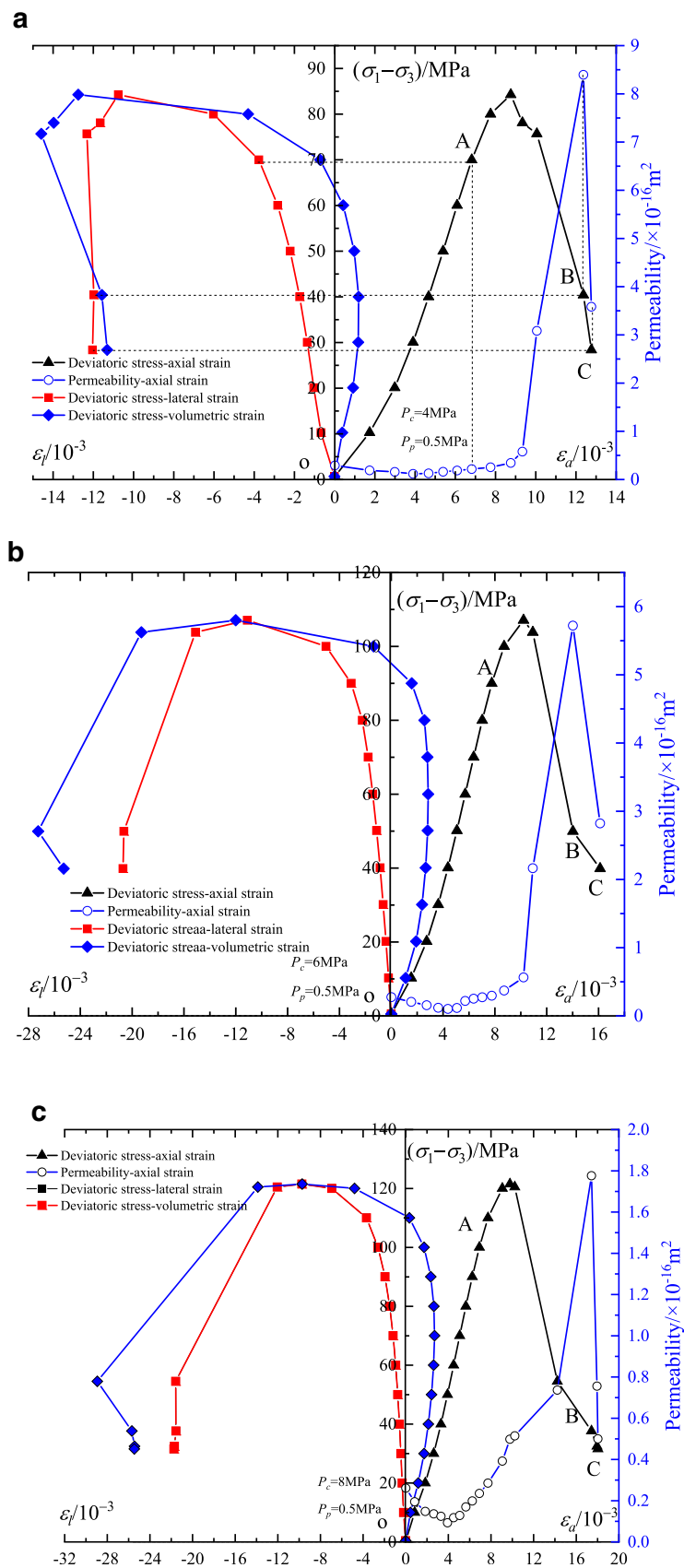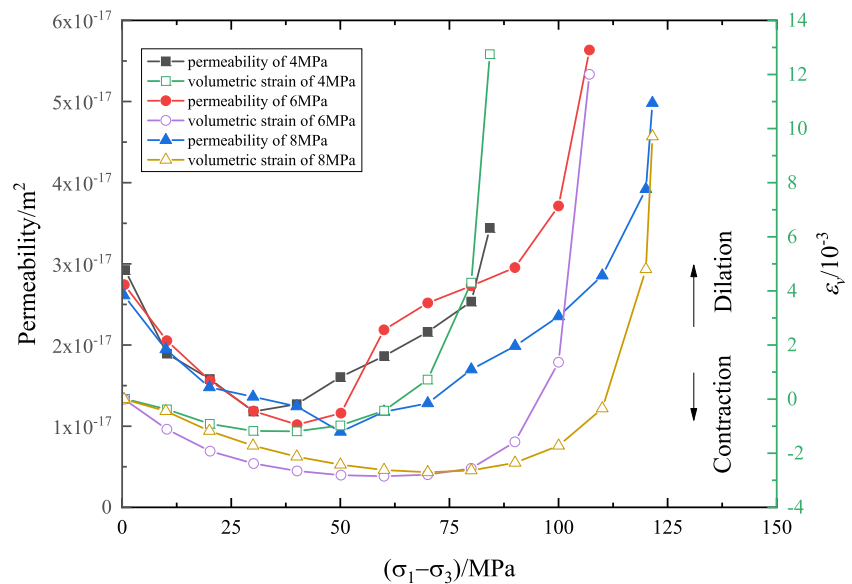$$\varepsilon_v = \varepsilon_a + 2\varepsilon_l \qquad (16)$$

Fig. 7 The variation of deviatoric stress and permeability with strain under different effective confining pressures

Fig. 8 The relationship between permeability and volumetric strain before peak stress. Both permeability and volumetric strain are plotted versus deviatoric stress

where ε_v, ε_a, and ε_l are the volumetric strain, axial strain, and lateral strain, respectively. From previous study, we can see that the permeability can vary by several orders of magnitude if the sandstone sample loses its bearing capacity. In order to analyze the permeability during the process of crack propagation, the variation of permeability with the increase of volumetric strain before the peak stress is plotted in Fig. 8. In Fig. 8, the dilation of volumetric strain is set as positive. The deviatoric stress–permeability relationships are similar to the stress–volumetric strain curves. Both permeability and volumetric strain under different effective confining pressures initially decrease up to the turning point, at which they then decrease at an accelerated rate. The inflection points of volumetric strain for effective confining pressures of 3.5, 5.5, and 7.5 MPa are about 40, 60, and 70 MPa, respectively. The turning points of permeability, however, do not coincide with the inflection points of the strain–stress, which are about 30, 40, and 50 MPa, respectively. This rule was also found in granodiorite by Mitchell and Faulkner (2008) and coal by Wang et al. (2013). Mitchell and Faulkner (2008) suggested that, as deviatoric stress was applied, cracks perpendicular to axial continue to close, while newly formed cracks grow parallel to axial. The new dilatant cracks contribute more to axial permeability than compaction radial cracks. In this paper, we can see that the propagation of microcracks has a great effect on the increasing of permeability. Brace et al. (1966) suggested that dilation can be attributed to the microcracks prior to failure. The onset of dilatancy marks the initiation of microcracks propagation or proliferation. This point can be marked by the stress state at which the volumetric strain deviates from the linear variation. The onset of dilatancy values of effective confining pressures of 3.5, 5.5, and 7.5 MPa are about 30, 40, and 50 MPa, respectively, which coincide well with the turning point of permeability.

Comparison between permeability under hydrostatic compaction and triaxial deformation

The relationship between permeability and effective confining pressure under hydrostatic compaction can be described by an exponential relationship. However, permeability, under triaxial deformation, is not only influenced by effective confining pressure, but also deviatoric stress. As a porous media, the sandstone samples only go through the process of initial defects compression and rearrangement of grains under hydrostatic compaction. Therefore, the permeability decreases monotonously with the increase of effective confining pressure. Moreover, when the hydrostatic pressure is greater, the initial defects are very hard to compress, so the permeability decreases slowly. Some researchers (David et al. 1994; Dewhurst et al. 1998; Zhu and Wong 1997) suggested that, when the effective confining pressure exceeds the turning point, rock grains are crushed. This is called "pore collapse", where the permeability reduces quickly. For permeability under triaxial deformation, the initial permeability variation is similar to the hydrostatic compaction condition, due to the influence of only effective confining pressure. When the deviatoric stress is not higher, the closing of cracks leads to the decrease of permeability. When the deviatoric stress is close to the value of the onset of dilatancy, the propagation of newly formed cracks leads to the increase of permeability. The cracks continue to coalesce with the applied deviatoric stress, and the permeability of sandstone samples transforms from pore seepage to fracture seepage. The peak value of permeability appears after the failure of samples.

Conclusion

In this paper, permeability of sandstone was tested during hydrostatic compaction and triaxial deformation. The

confining pressures under the triaxial deformation condition were 4, 6, and 8 MPa, respectively. The upstream pressure was 1 MPa. The confining pressures under hydrostatic compaction increased from 2 to 20 MPa with an upstream pressure of 1 MPa. In order to make a comparison with the water test results, the permeability and porosity were also measured using argon during hydrostatic compaction. The results are as follows.

Both water permeability and gas permeability decrease with the increase of effective confining pressure during the hydrostatic compaction. The gas permeability, however, is almost one order of magnitude lager than the water permeability at the same stress. This is induced by the slippage effect, which adds an additional value to the measured gas permeability.

The slippage factor, which represents the impact of the slippage effect on the permeability measured by gas, can be concluded from the equation $b \propto (K_\infty/\varphi)^{-0.5}$. The gas permeability was, then, modified by this equation. The modified gas permeability is close to but less than the water permeability. This trend can be explained by the following: (1) water can dissolve matrixes of sandstone, which expands the pore throat radius; (2) gas viscosity is closely related to pore pressure, which increases the gas permeability.

A fitting process was conducted on the water permeability and modified gas permeability. The results indicated that an exponential relationship $K = K_0 \, exp\,[-\gamma(P_e - P_0)]$ is superior to a power law for describing the stress-dependent permeability. A power law $\varphi = \varphi_0 (P_e/P_0)^{-\theta}$, however, is more appropriate for describing the relationship between porosity and effective confining pressure.

The permeability–axial strain curves of sandstone are roughly in accordance with the deviatoric stress–axial strain curves and can be divided into three stages. During the first stage, the permeability is very low. During the second stage, the permeability increases rapidly and reaches its peak value in the strain-softening stage. During the third stage, the permeability decreases and reaches an ultimate stabilized level.

Under triaxial compression, the permeability rule with the increase of deviatoric stress is similar to the volumetric deformation before the peak stress. However, the lowest value of permeability occurs before the inflection point, at which samples start to dilate. The propagation of microcracks has a great effect on the increase of permeability. The turning point of permeability coincides well with the onset of dilatancy, which marks the initiation of microcracks propagation or proliferation.

Permeability variation is so complicated due to the effect of not only the effective confining pressure but also the deviatoric stress during triaxial deformation. However, all of the initial permeability, lowest permeability, peak permeability, and stable value of permeability decrease with the increase of effective confining pressure.

References

Alam AB, Niioka M, Fujii Y, Fukuda D, Kodama J-i (2014) Effects of confining pressure on the permeability of three rock types under compression. Int J Rock Mech Min Sci 65:49–61

Athy LF (1930) Density, porosity, and compaction of sedimentary rocks. AAPG Bull 14:1–24

Brace WF, Paulding BW Jr, Scholz CH (1966) Dilatancy in the fracture of crystalline rocks. J Geophys Res 71:3939–3953

Chen L, Liu JF, Wang CP, Liu J, Su R, Wang J (2014) Characterization of damage evolution in granite under compressive stress condition and its effect on permeability. Int J Rock Mech Min Sci 71:340–349. https://doi.org/10.1016/j.ijrmms.2014.07.020

Civan F (2010) Effective correlation of apparent gas permeability in tight porous media. Transp Porous Media 82:375–384. https://doi.org/10.1007/s11242-009-9432-z

David C, Wong TF, Zhu WL, Zhang JX (1994) Laboratory measurement of compaction-induced permeability change in porous rocks: implications for the generation and maintenance of pore pressure excess in the crust. Pure Appl Geophys 143:425–456. https://doi.org/10.1007/Bf00874337

Dewhurst DN, Aplin AC, Sarda JP, Yang Y (1998) Compaction-driven evolution of porosity and permeability in natural mudstones: an experimental study. J Geophys Res Solid Earth 103:651–661

Dong JJ, Hsu JY, Wu WJ, Shimamoto T, Hung JH, Yeh EC, Wu YH, Sone H (2010) Stress-dependence of the permeability and porosity of sandstone and shale from TCDP Hole-A. Int J Rock Mech Min Sci 47:1141–1157. https://doi.org/10.1016/j.ijrmms.2010.06.019

Duan Z, Davy CA, Agostini F, Jeannin L, Troadec D, Skoczylas F (2014) Gas recovery potential of sandstones from tight gas reservoirs. Int J Rock Mech Min Sci 65:75–85. https://doi.org/10.1016/j.ijrmms.2013.11.011

Evans JP, Forster CB, Goddard JV (1997) Permeability of fault-related rocks, and implications for hydraulic structure of fault zones. J Struct Geol 19:1393–1404. https://doi.org/10.1016/S0191-8141(97)00057-6

Florence FA, Rushing J, Newsham KE, Blasingame TA (2007) Improved permeability prediction relations for low permeability sands. In: Proceedings of the Rocky Mountain Oil & Gas Technology Symposium, Denver, Colorado, April 2007. Society of Petroleum Engineers. https://doi.org/10.2118/107954-MS

Ghabezloo S, Sulem J, Guédon S, Martineau F (2009) Effective stress law for the permeability of a limestone. Int J Rock Mech Min Sci 46:297–306. https://doi.org/10.1016/j.ijrmms.2008.05.006

Heid J, McMahon J, Nielsen R, Yuster S (1950) Study of the permeability of rocks to homogeneous fluids. In: Drilling and production practice. American Petroleum Institute, New York

Heiland J, Raab S (2001) Experimental investigation of the influence of differential stress on permeability of a Lower Permian (Rotliegend) sandstone deformed in the brittle deformation field. Phys Chem Earth A Solid Earth Geodesy 26:33–38. https://doi.org/10.1016/S1464-1895(01)00019-9

Hoholick JD, Metarko T, Potter PE (1984) Regional variations of porosity and cement: St. Peter and Mount Simon sandstones in Illinois Basin. AAPG Bull 68:753–764

Jones FO, Owens WW (1980) A laboratory study of low-permeability gas sands. J Pet Technol 32:1631–1640

Klinkenberg L (1941) The permeability of porous media to liquids and gases. In: Drilling and production practice. American Petroleum Institute, New York, pp 200–213

Lion M, Skoczylas F, Ledésert B (2004) Determination of the main hydraulic and poro-elastic properties of a limestone from Bourgogne, France. Int J Rock Mech Min Sci 41:915–925. https://doi.org/10.1016/j.ijrmms.2004.02.005

Liu Z, Shao J (2017) Strength behavior, creep failure and permeability change of a tight marble under triaxial compression. Rock Mech Rock Eng 50:529–541

Liu ZB, Xie SY, Shao JF, Conil N (2017) Multi-step triaxial compressive creep behaviour and induced gas permeability change of clay-rich rock. Geotechnique 68:281–289

Loosveldt H, Lafhaj Z, Skoczylas F (2002) Experimental study of gas and liquid permeability of a mortar. Cem Concr Res 32:1357–1363. https://doi.org/10.1016/S0008-8846(02)00793-7

Mitchell TM, Faulkner DR (2008) Experimental measurements of permeability evolution during triaxial compression of initially intact crystalline rocks and implications for fluid flow in fault zones. J Geophys Res Solid Earth 113(B11). https://doi.org/10.1029/2008jb005588

Sampath K, Keighin CW (1982) Factors affecting gas slippage in tight sandstones of cretaceous age in the Uinta basin. J Pet Technol 34:2715–2720

Schmoker JW, Halley RB (1982) Carbonate porosity versus depth: a predictable relation for south Florida. AAPG Bull 66:2561–2570

Shi YL, Wang CY (1988) Generation of high pore pressures in accretionary prisms: inferences from the Barbados subduction complex. J Geophys Res Solid Earth 93:8893–8910. https://doi.org/10.1029/JB093iB08p08893

Tanikawa W, Shimamoto T (2009) Comparison of Klinkenberg-corrected gas permeability and water permeability in sedimentary rocks. Int J Rock Mech Min Sci 46:229–238

Wang SG, Elsworth D, Liu JS (2013) Permeability evolution during progressive deformation of intact coal and implications for instability in underground coal seams. Int J Rock Mech Min Sci 58:34–45. https://doi.org/10.1016/j.ijrmms.2012.09.005

Wang HL, Xu WY, Shao JF (2014a) Experimental researches on hydromechanical properties of altered rock under confining pressures. Rock Mech Rock Eng 47:485–493. https://doi.org/10.1007/s00603-013-0439-y

Wang HL, Xu WY, Zuo J (2014b) Compact rock material gas permeability properties. Physica B Condens Matter 449:10–18. https://doi.org/10.1016/j.physb.2014.04.049

Wang L, Liu JF, Pei JL, Xu HN, Bian Y (2015) Mechanical and permeability characteristics of rock under hydro-mechanical coupling conditions. Environ Earth Sci 73:5987–5996. https://doi.org/10.1007/s12665-015-4190-4

Wang Y, Agostini F, Skoczylas F, Jeannin L, Portier É (2017) Experimental study of the gas permeability and bulk modulus of tight sandstone and changes in its pore structure. Int J Rock Mech Min Sci 91:203–209. https://doi.org/10.1016/j.ijrmms.2016.11.022

Wu YQ, Zhang ZY (1995) Introduction to rock mass hydraulics. Southwest Jiaotong University Press, Chengdu

Yuan HF, Agostini F, Duan ZB, Skoczylas F, Talandier J (2017) Measurement of Biot's coefficient for COx argillite using gas pressure technique. Int J Rock Mech Min Sci 92:72–80. https://doi.org/10.1016/j.ijrmms.2016.12.016

Zhu WL, Wong TF (1996) Permeability reduction in a dilating rock: network modeling of damage and tortuosity. Geophys Res Lett 23:3099–3102. https://doi.org/10.1029/96gl03078

Zhu WL, Wong TF (1997) The transition from brittle faulting to cataclastic flow: permeability evolution. J Geophys Res Solid Earth 102:3027–3041. https://doi.org/10.1029/96jb03282

Zoback MD, Byerlee JD (1975) Permeability and effective stress: geologic notes. AAPG Bull 59:154–158